

## Exploring human carboxylesterases 1 and 2 selectivity of two families of substrates at an atomistic level

Sergio R. Ribone <sup>a,b</sup>, Dario A. Estrin <sup>c,d</sup>, Mario A. Quevedo <sup>a,b,\*</sup>

<sup>a</sup> Universidad Nacional de Córdoba, Facultad de Ciencias Químicas, Departamento de Ciencias Farmacéuticas, Haya de la Torre esq. Medina Allende, Ciudad Universitaria, Córdoba 5000, Argentina

<sup>b</sup> Consejo Nacional de Investigaciones Científicas y Técnicas (CONICET), Unidad de Investigación y Desarrollo en Tecnología Farmacéutica (UNITEFA), Haya de la Torre esq. Medina Allende, Ciudad Universitaria, Córdoba 5000, Argentina

<sup>c</sup> Universidad de Buenos Aires, Facultad de Ciencias Exactas y Naturales, Departamento de Química Inorgánica, Analítica y Química Física, Intendente Güiraldes 2160, C1428EHA Buenos Aires, Argentina

<sup>d</sup> Consejo Nacional de Investigaciones Científicas y Técnicas (CONICET), Instituto de Química Física de los Materiales, Medio Ambiente y Energía (INQUIMAE), Ciudad Universitaria, Pabellón 2, Ciudad Autónoma de Buenos Aires, C1428EHA Buenos Aires, Argentina

### ARTICLE INFO

#### Keywords:

CES1A1  
CES2A1  
Substrates specificity  
Classical MD simulations  
Hybrid QM/MM simulations  
*P*-nitrophenyl ester  
Pyrethroid stereoisomers

### ABSTRACT

Human carboxylesterases (CES) are enzymes that play an important role in the metabolism and biotransformation of diverse substances. The two more relevant isoforms, CES1A1 and CES2A1, catalyze the hydrolysis of numerous approved drugs and prodrugs. The elucidation of CES isoform substrates specificity constitutes a very relevant medicinal chemistry issue. The general role pointed that the selectivity towards CES1A1 or CES2A1 depends on the size of the acyl and alkyl moieties present in the structure of the substrate, but several exceptions regarding substrate promiscuity towards both CES have been reported. In this work, a combination of classical molecular dynamics (MD) and hybrid quantum mechanics/molecular mechanics (QM/MM) simulations were applied with the purpose of studying the substrate selectivity of CES1A1 and CES2A1 on two sets of selected ligands: *p*-nitrophenyl ester derivatives (NPE) and pyrethroid stereoisomers (Pyr). The classical molecular modeling studies showed that the van der Waals (VDW) component of interaction, with the hydrophobic residues present on CES1A1 and CES2A1 subpocket 1 and subpocket 2, showed a significant contribution to the substrates-CES affinity properties. The hybrid QM/MM simulations exhibited that the rate-limiting step for the studied substrates reactions were related to the transition state (TS) with the higher steric hindrance molecular structure. In conclusion, it was possible to observe that the studied substrates generate the best possible interaction pattern with the residues from subpocket 1 and 2 in order to produce the corresponding affinity constant with the enzyme. Then, this interaction pattern drives the catalytic turn-over reaction through the presence or absence of a high steric hindrance center in the molecular structure of the rate-limiting reaction.

### 1. Introduction

Human carboxylesterases (CES) are members of the serine hydrolase superfamily of enzymes [1,2] that play an important role in the metabolism and biotransformation of diverse endogenous and exogenous substances, among which carboxylic acid derivatives (i.e. esters, thioesters, amides and carbamates) represent the main substrates. [3,4] Five CES families have been described to date (i.e. CES1 to CES5), [4] however two of them, CES1A1 and CES2A1 isoforms, are the more relevant from a clinical point of view. [5,6] In this respect, both CES1A1

and CES2A1 are responsible for catalyzing several key biological processes, modulating the esterification levels of cholesterol, triacylglycerols and other endogenous lipids. [7–9] CES also mediates biotransformation (i.e. metabolism and/or bioactivation) of exogenous compounds, among which therapeutically relevant drug constitutes clinically relevant examples.

CES1A1 and CES2A1 share 47 % of protein sequence identity, exhibiting not only different substrate specificity but also differential tissue distribution. [4,10–12] In this respect, it has been reported that CES1A1 is mainly expressed in liver, while CES2A1 is mostly present in

\* Corresponding author at: Universidad Nacional de Córdoba, Facultad de Ciencias Químicas, Departamento de Ciencias Farmacéuticas, Haya de la Torre esq. Medina Allende, Ciudad Universitaria, Córdoba 5000, Argentina.

E-mail address: [aquevedo@unc.edu.ar](mailto:aquevedo@unc.edu.ar) (M.A. Quevedo).

the intestine. [3,4]

Available crystallographies show that the structure of CES can be divided in three main functional domains: the catalytic domain, the  $\alpha/\beta$  domain and the regulatory domain. [1,13] In both CES isoforms, the catalytic site is located within the catalytic domain, including the classical Ser-His-Glu triad, typical of the serine hydrolase family (Ser221-His467-Glu354 and Ser228-His457-Glu345 for CES1A1 and CES2A1, respectively). [1,13] Also, an oxyanion hole region is present within the catalytic site, lined by residues Gly142-Gly143-Ala222 and Gly149-Ala150-Ala229 in CES1A1 and CES2A1, respectively. [1,13]

The substrate selectivity of both enzymes has been analyzed in terms of two main kinetic parameters: 1) the affinity constant ( $K_M$ ), which is related to the affinity of the substrate for the binding site, [14,15] and 2) the catalytic turn-over constant ( $k_{cat}$ ), [14,15] which describes the rate of hydrolysis produced by the enzyme over the substrate. The ratio between both parameters ( $k_{cat}/K_M$ ) is known as the *catalytic efficiency* (CE). [14,15] A high CE, originated from a good catalytic reaction rate and a low affinity constant, indicates that the ligand is an excellent substrate for the enzyme.

Overall, it has been generally accepted that CES substrate binding selectivity to each isoform is determined mainly by the size and physicochemical properties of the acyl and alkyl moieties of the corresponding ligands. In this way, CES1A1 has been pointed to preferentially catalyze the hydrolysis of substrates bearing smaller alkyl than acyl groups in their structure, which is the case for numerous approved drugs and prodrugs, such as meperidine, lidocaine, methylphenidate, imidapril, temocapril, oseltamivir and clopidogrel, among others. [3,5,6,16]. On the other hand, compounds with smaller acyl than alkyl moieties are more likely to constitute substrates of CES2A1, among which some therapeutically relevant examples such as procaine, flutamide, *N*-acetyldapsone, prasugrel, haloperidol ester, can be mentioned. [3–6,16].

Although some studies have been addressed to further explore this general rule, [6,17] several exceptions regarding substrate promiscuity towards both CES isoforms have been reported in the literature, [14,16,18–22] with drugs and prodrugs such as prilocaine, propanil, oxybutinin and irinotecan constituting relevant examples of unselectively metabolized therapeutics agents. [16,21,22] In addition, a widely reported exception to the above mentioned general rule is heroin, which is mainly metabolized by CES1A1 regardless of the presence of a larger alkyl moiety respect to the acyl structure. [18]

The complexity of the atomistic events driving CES isozyme recognition is further extended by the stereoselectivity observed for each isoenzyme. In this respect, a remarkable example is represented by the differential CES mediated biotransformation rates reported several pyrethroid compounds. [19] Specifically, Yang et al. reported that the *cis* and *trans* isomers of permethrin displayed different CES1A1 and CES2A1 hydrolysis rates, even though they present similar sizes of acyl and alkyl groups. In particular, *trans*-permethrin is efficiently hydrolyzed by both CES isoforms, while *cis*-permethrin is hydrolyzed mainly by CES2A1. [19] An homologous phenomena was reported in the study of the different hydrolysis pattern for the eight cypermethrin and four fenvalerate stereoisomers [14].

In this scenario, and given the biological importance of CES mediated catalysis, further exploring the structural basis governing CES isoform substrates specificity constitutes a very relevant scientific issue, providing valuable insights for the design of drugs and prodrugs with optimized biopharmaceutical profiles. Among them, avoiding unwanted early biotransformation of the prodrugs and/or designing their site-specific bioactivation has been envisioned as a promising strategy upon targeting particular CES isoforms. [1,4,12]. A relevant example are amide derived prodrugs of Gemcitabine used for the treatment of solid tumors, which are selectively bioactivated by CES2A1 overexpressed in certain type of cancers. [23–25] Also, the design of CES1A1 and CES2A1 specific inhibitors constitute an interesting approach for the management of certain metabolic diseases, with the CES1A1 inhibitor

GR148672X being currently under preclinical development as a candidate to treat hypertriglyceridemia, obesity and atherosclerosis. [26–28]

Considering that it is clear that CES binding and hydrolysis encompasses subtle intermolecular interaction events exceeding the general currently accepted rule focused on the size of the alkyl and acyl scaffolds, in this work, a combination of classical molecular dynamics and hybrid QM/MM computer aided simulations were applied with the purpose of studying at an atomistic level CES1A1 and CES2A1 substrate selectivity. The *in silico* methods combined classical MM strategies to describe substrate binding to the catalytic site ( $K_M$ ) by applying molecular docking protocols, classical molecular dynamic simulations (MD) and interaction free-energy analyses. In order to model the enzymatic turnover ( $k_{cat}$ ), the hydrolytic reaction coordinate was studied by means of hybrid QM/MM-MD simulations, both including five well known CES substrates belonging to the family of *p*-nitrophenyl ester derivatives (NPE) selected based on availability of kinetic data, [15] and two more complex structural substrates belonging to the family of pyrethroid stereoisomers (Pyr). [14] Overall, an agreement between our calculations and experimental observations was found, demonstrating the utility of the applied workflow towards unravelling the molecular details related to the different enzyme turnover process elicited by both CES isoforms.

## 2. Results and discussion

### 2.1. Comparison of CES1A1 and CES2A1 catalytic sites

A comparative analysis of CES1A1 and CES2A1 molecular structure, as well as the corresponding catalytic sites, was performed prior to evaluating substrate recognition and binding. For this analysis, the crystallographic structure of CES1A1 (PDB code 5A7F) was used, while an homology model structure of CES2A1 was retrieved from SWISS-MODEL server based on the template structure of CES1A1, due to the absence of a reported crystal structure of CES2A1. The superimposition of both structures exhibited their high structural homology, especially within the region corresponding to the catalytic sites (Fig. 1a). Noteworthy, the main difference among the two aligned structures arises from the presence of a large loop located at the entrance of CES1A1 catalytic site, fact that has been already reported. [13] This loop limits the surface availability of substrates in the active site of CES1A1, while its absence in CES2A1 results in a higher exposure of the cavity (Fig. 1b and c).

Respect to the catalytic site cavity, differences in shape and size were calculated using the POVME software [29]. The geometric centre of reference was placed on the oxygen atom of the catalytic serine residue (Ser221 and Ser228 for CES1A1 and CES2A1, respectively). The overall available surface is presented in (Fig. 2a), which clearly shows a higher volume for CES2A1 (285 Å<sup>3</sup> and 365 Å<sup>3</sup> for CES1A1 and CES2A1, respectively), feature that is not only observed for the solvent exposed region, but also for the buried subcavities. Further inspection of the calculated accessibility spheres indicates that both cavities are spatially divided into four discrete subregions (Fig. 2b), three of which delineates the substrate binding subpocket (subpockets 1, 3 and 4), while the fourth region encompasses an interconnection channel between the solvent exposed and the buried regions of the catalytic site (subpocket 2). Numbering of these regions was arbitrarily assigned considering the distance of the corresponding center of mass. As can be seen, the superimposition of these four regions on both isoenzymes shows that all of them exhibit a higher volume in CES2A1 compared to CES1A1.

When the structure of CES1A1 is analyzed, subpocket 1 is oriented towards the opposite side of the catalytic site cavity, lined by residues Val254, Leu255, Leu304, Leu318, Ile359, Leu362, Met363, Leu387, Met424 and Phe425, exhibiting an apolar environment with the highest available volume. In counterpart, subpocket 2 exhibits the lowest surface among all cavities, and is lined by the catalytic residues Ser221 and His467 and the residues comprising the oxyanion hole (Gly142, Gly143

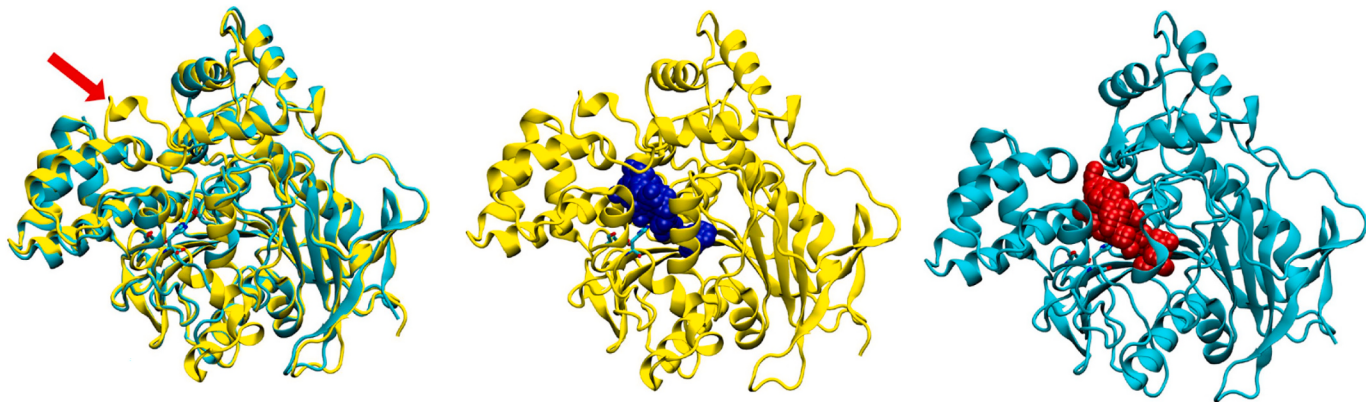


**Fig. 1.** CES1A1 (yellow) and CES2A1 (cyan) structural superimposition, red arrow indicating the presence of CES1A1 loop (a). CES1A1 structure (yellow) and calculated catalytic site cavities (blue spheres) (b) CES2A1 structure (cyan) and calculated catalytic site cavities (red spheres) (c). (For interpretation of the references to colour in this figure legend, the reader is referred to the web version of this article.)

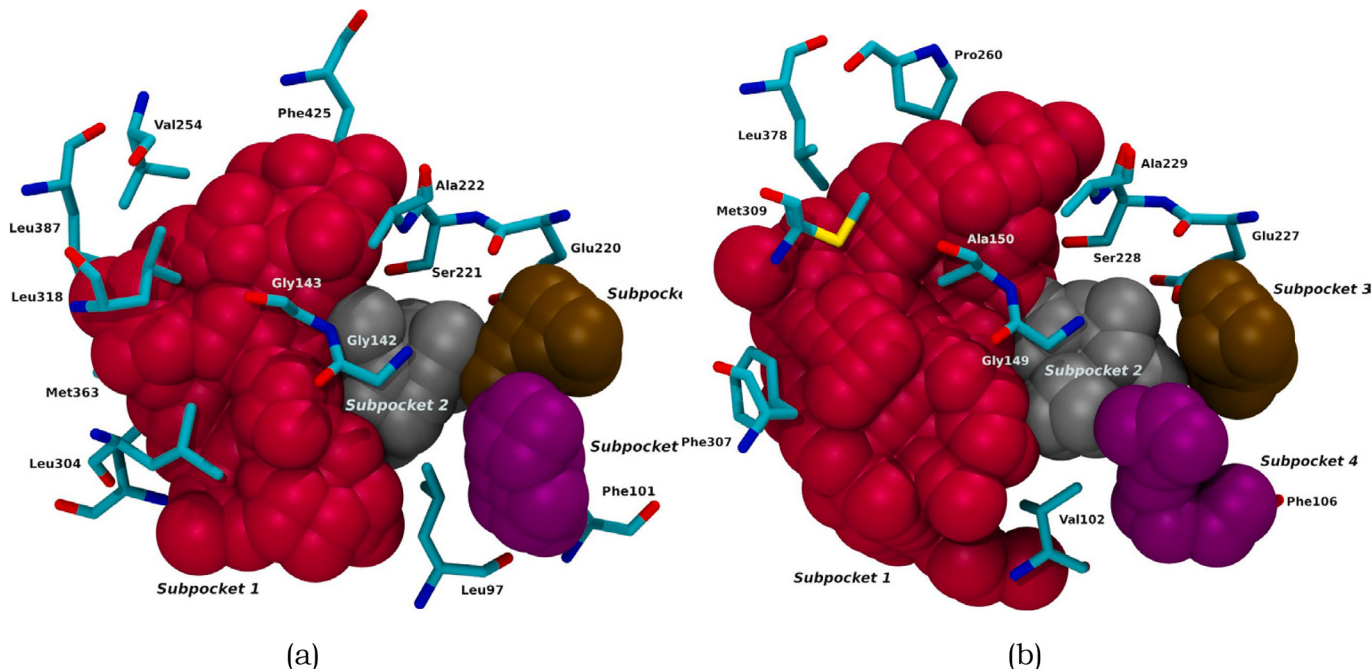


**Fig. 2.** Top view on CES1A1 (a) and CES 2 (b) calculated catalytic site cavities divided in four subregions: Subocket 1 (red), Subocket 2 (silver), Subocket 3 (ochre) and Subocket 4 (purple) with their respective residues (licorice representation). (For interpretation of the references to colour in this figure legend, the reader is referred to the web version of this article.)

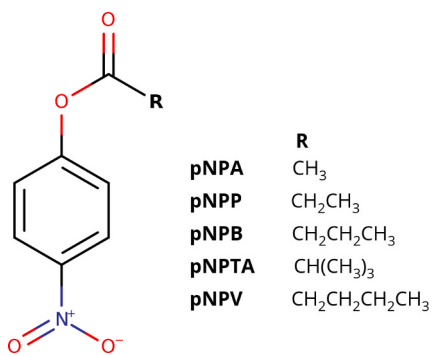
and Ala222). In this way, an efficient spatial orientation of the scissile bond of substrates within this region is anticipated as critical for the catalysis to occur. Finally, subocket 3 is formed by residues Trp145, His147, Gly148, Leu158 and Tyr159, while subocket 4 is lined by residues Phe153, Pro260, Phe307, Met309, Ile350, Val353, Met354, Leu378, Met415 and Phe416 (Figure S1A).

CES2A1 presents an homologous topology, with subocket 2 also placed in the center of the catalytic domain and lined by residues comprising the catalytic triad (Ser228 and His457) and the oxyanion hole (Gly149, Ala150 and Ala229)(Figure S1B). When compared to CES1A1, the main difference in this subocket arises from the replacement of Leu97 (CES1A1) for Val102 (CES2A1), resulting in a wider channel for the latter. With respect to subocket 3, it is lined by residues Trp145, His147, Gly148, Leu158 and Tyr159, while subocket 4 is formed by residues Phe153, Pro260, Phe307, Met309, Ile350, Val353, Met354, Leu378, Met415 and Phe416 (Figure S1B).

## 2.2. Modeling of the intermolecular recognition between CES isoforms and the NPE derivatives

### 2.2.1. Selection of NPE substrates

The selection of the substrates was based on the existence of reported kinetic parameters ( $K_M$  and  $k_{cat}$ ) associated with in vitro CES hydrolysis. In this way, the selected compounds corresponded to the well known CES substrates belonging to the *p*-nitrophenyl ester (NPE) derivatives (Fig. 3), which have been vastly reported to be CES substrates. [15] As can be seen, a strong dependency on  $K_M$  is observed as the size of the acyl chain increases. On the other hand, there is not an evident correlation between the substrate structures and the  $k_{cat}$ , however in all cases the enzymatic turnover is higher for CES2A1 respect to CES1A1. In addition, the molecular simplicity of these derivatives represents a benefit in terms of computational cost for the hybrid QM/MM-MD simulation studies. Consequently, this set of compounds constitute excellent



Substrate	$K_M^a$		$k_{cat}^b$		$k_{cat}/K_M^c$	
	CES1A1	CES2A1	CES1A1	CES2A1	CES1A1	CES2A1
pNPA	822±73	976±60	3.1±0.5	23.4±2.4	3.8±0.3	24±1
pNPP	249±9	201±18	7.9±0.4	52.5±6.1	32±0.6	261±7
pNPB	169±8	117±5	6.3±0.5	67.9±3.5	37±1	580±5
pNPTA	29±5	19.8±1.1	0.4±0.1	4.4±0.4	15±0.6	220±9
pNPV	27±2.7	71±11	1.4±0.2	29.9±6.5	52±2.5	421±27

<sup>a</sup>  $\mu M$ , <sup>b</sup>  $s^{-1}$ , <sup>c</sup>  $mM^{-1}$ .

**Fig. 3.** Molecular structure of the *p*-nitrophenyl ester (NPE) derivatives family with their respective CES kinetic parameters. [15].

molecular probes to develop the modeling protocol reported in this work.

Substrate	$K_M^a$		$k_{cat}^b$		$k_{cat}/K_M^c$	
	CES1A1	CES2A1	CES1A1	CES2A1	CES1A1	CES2A1
pNPA	822±73	976±60	3.1±0.5	23.4±2.4	3.8±0.3	24±1
pNPP	249±9	201±18	7.9±0.4	52.5±6.1	32±0.6	261±7
pNPB	169±8	117±5	6.3±0.5	67.9±3.5	37±1	580±5
pNPTA	29±5	19.8±1.1	0.4±0.1	4.4±0.4	15±0.6	220±9
pNPV	27±2.7	71±11	1.4±0.2	29.9±6.5	52±2.5	421±27

<sup>a</sup>  $\mu M$ , <sup>b</sup>  $s^{-1}$ , <sup>c</sup>  $mM^{-1}$ .

#### 2.2.2. Binding of NPE family to CES1A1 and CES2A1

In order to study at an atomistic level the substrate binding recognition and the corresponding intermolecular interactions, the previously mentioned NPE substrates were docked to both CES isoforms, identifying the lowest energy docked pose.

The predicted binding poses showed similar spatial dispositions within the catalytic site cavity of both CES isoforms, positioning the carbonyl oxygen of the hydrolyzable ester moiety in the region corresponding to the oxyanion hole (subpocket 2), thus establishing hydrogen bond interactions with the corresponding residues (Figure S2-S11). The alkyl moiety (nitrophenyl scaffold) of all NPE derivatives was positioned within subpocket 1, establishing hydrophobic interactions within the subpocket residues, while the acyl substituents were placed within subpocket 2 of the catalytic site (Figure S2-S11). As is presented, no significant differences were observed in the binding mode to CES isoforms, which is consistent with the non subtype selective hydrolysis observed for this set of compounds.

In order to exhaustively explore the conformational evolution of the intermolecular complexes described above, all structures were subjected to explicit solvent classic MD simulations. Figs. S12a and S12b show the computed distances between the center of mass of the CES1A1 and CES2A1 catalytic binding sites and the bounded substrates, respectively. This analysis displayed that all the studied NPE ligands maintained their position within both CES active sites throughout the 100 ns of production stage. The larger distance observed for CES2A1 respect to CES1A1 are originated in the larger size of CES2A1 active site. With these CES-NPE MD simulations, further free-energy of binding interaction (MMGBSA) analyses were applied.

#### 2.2.3. Free-energy interaction analysis

The free-energy binding interaction analysis on the MD trajectories of the CES-NPE complexes exhibited a correlation with the reported experimental studies. [15] Table 1 exhibits a trend between the experimental affinity constant ( $K_M$ ) and the total free-energy of interaction ( $\Delta G_{Total}$ ), where pNPA displayed the lowest  $\Delta G_{Total}$  of interaction and the lowest affinity constant in opposition of pNPV that showed the highest  $\Delta G_{Total}$  of interaction and the highest affinity constant. An exception of this relationship was pNPTA. This NPE derivative displayed a higher  $\Delta G_{Total}$  of interaction than the expected which is originated in the smaller solvent accessible surface area of the bulkier trimethyl acetate moiety, generating the highest solvation polar contribution ( $\Delta G_{polar}$ ). In addition, the NPE substrates with the larger affinity constants displayed the higher van del Waals (VDW) interaction component, exhibiting a significant contribution to the NPE-CES interaction.

A similar observation was previously reported, [15] where they found a correlation between the experimental  $K_M$  and the calculated water/octanol partition coefficients (clogP) values from the NPE series. The authors asseverated that the reason for this relationship was that the presence of longer and more hydrophobic alkyl chain esters improved the interaction with the residues of the active site, which is lined mainly by hydrophobic residues.

In order to inspect the active site residues interaction pattern, a per-residue free-energy decomposition analysis was performed for all the CES1A1 and CES2A1-substrates complexes. Fig. 4 show the free-energy per-residue decomposition analysis obtained for both CES and NPE complexes, with the total free-energy active site residues sum at the bottom of the graphics. In this study, the residues from the catalytic triad and the oxyanion hole were not included in the analysis, since very similar interaction values were found.

The NPE derivatives displayed free-energy interactions mainly with residues from subpocket 1 and subpocket 2 of CES1A1 (Leu97, Phe101, Glu220, Leu304, Ile359 and Phe425) and CES2A1 (Phe106, Glu227, Ile350, Val353, Met354 and Phe416). Fig. 4 showed a trend between the number of interactions established within subpocket 1 and subpocket 2 and the experimental affinity constant, with larger values being observed for ligands able to contact a higher number of residues.

#### 2.3. Hybrid QM/MM simulation of the NPE substrates

In this section, the study of the potential of mean force (PMF) involved in the hydrolysis reaction with both CES enzymes was evaluated in order to model the corresponding reaction coordinate. For this purpose, two members of the NPE family were selected, the substrates with the lower and higher reported enzymatic turnovers for CES1A1 and lower and second higher reported enzymatic turnovers for CES2A1 (pNPTA and pNPP, respectively). [15]

Following a previous report in which the hydrolysis mechanism of cocaine by CES1A1 was studied, [1] a two step hydrolysis mechanism was proposed: 1) acylation and 2) deacylation stages on the reaction of the selected ligands by CES1A1 and CES2A1 (Fig. 5).

#### 2.3.1. Acylation reaction

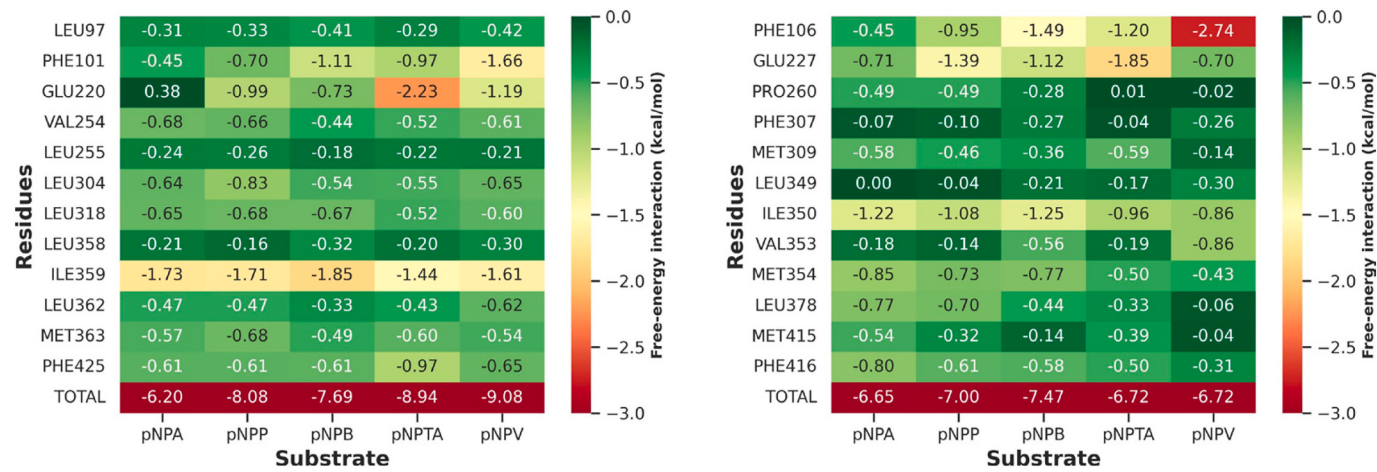
Using the encounter complex obtained from the hydrogen bond restrained QM/MM MD simulation as the starting point for the acylation stage, the QM/MM (SCC-DFTB3:Amberff14SB) reaction coordinate involving four distances was employed in an umbrella sampling calculation, in which two bonds were formed during the reaction and two bonds were broken (Fig. 5). The catalytic Ser hydroxyl hydrogen atom approached the catalytic His nitrogen atom (D1, Fig. 5) and moved away from its hydroxyl oxygen atom bond (D2, Fig. 5). Concurrently, the Ser hydroxyl oxygen atom attacks the carbonyl carbon atom of the ester substrate until a covalent bond is formed (D3, Fig. 5) and the ester bond between the oxygen atom and the carbonyl carbon atom from the ester ligands moves away, resulting in covalent bond breaking (D4, Fig. 5). These four bond lengths were combined in a linear combination of

**Table 1**

Free-energy interaction analysis for NPE derivatives on both CES1A1 and CES2A1.

Enzyme	Substrate	$K_M^a$	VDW <sup>b</sup>	ELE <sup>c</sup>	$\Delta G_{\text{nonpolar}}^d$	$\Delta G_{\text{polar}}^e$	$\Delta G_{\text{Total}}^f$
CES1A1	pNPA	822	-25.1±1.8	-20.8±2.2	-4.1±0.1	28.9±2.0	-21.1±2.2
	pNPP	249	-29.2±1.7	-19.0±2.4	-4.5±0.1	29.8±2.4	-22.8±2.4
	pNPB	169	-32.3±1.8	-20.0±2.7	-4.9±0.1	32.6±2.6	-24.6±2.5
	pNPTA	29	-31.9±2.1	-17.0±1.6	-4.9±0.1	36.1±1.8	-17.6±2.7
	pNPV	27	-34.8±2.1	-18.7±2.7	-5.2±0.2	30.4±2.2	-28.3±2.6
	pNPA	976	-25.3±1.7	-19.6±2.2	-3.9±0.1	29.2±2.3	-19.7±2.5
CES2A1	pNPP	201	-25.3±2.0	-17.9±2.4	-4.0±0.1	26.9±2.5	-20.4±2.8
	pNPB	117	-28.9±1.9	-16.1±2.3	-4.6±0.1	28.0±3.2	-21.5±2.9
	pNPTA	19.8	-28.4±1.8	-14.7±2.2	-4.2±0.1	32.3±2.2	-15.1±2.2
	pNPV	71	-33.6±1.9	-19.0±2.0	-5.0±0.1	33.9±2.1	-23.6±2.5

<sup>a</sup>μM. <sup>b</sup> Van der Waals contribution (kcal/mol). <sup>c</sup>Electrostatic contribution (kcal/mol). <sup>d</sup>Solvation non-polar contribution (kcal/mol). <sup>e</sup>Solvation polar contribution (kcal/mol). <sup>f</sup>Total binding free-energy (kcal/mol).

**Fig. 4.** Per-residue free-energy decomposition analysis heatmap from the CES1A1-NPE (a) and CES2A1-NPE complexes (b).

distances (LCOD), spanning from -4.0 to 4.0 range, to generate the reaction coordinate (RC) analysis according to eq. 1.

$$RC = D2 + D4 - D1 - D3 \quad (1)$$

The four distances were monitored during the course of the acylation reaction of all the analyzed substrates (D1, D2, D3 and D4, respectively, Figs. S13a, 13c, 14a and 14c).

Only one transition state ( $TS_1$ ) was present in the acylation reaction, starting from the reactive state (RS) and finishing in the intermediate state (INT), with the formation of the corresponding alcohol and the acylated enzyme (Fig. 5). Figs. S13a, S13c, S14a and S14c showed that D1 decreases until reaching  $TS_1$  (RC ~0.5) with a shortest distance of ~1.1 Å. Meanwhile, the distances between the carbonyl carbon atom and both oxygen atoms (Ser oxygen and ester oxygen atoms) were ~1.9 Å and ~1.5 Å, D3 and D4, respectively. Clearly, no covalent bond was formed between the carbonyl carbon and the oxygen atoms, indicating that the acylation reaction occurred following a concerted process, where one C—O bond is formed by nucleophilic attack and a second C—O bond was broken simultaneously, which is in agreement with the previous published study involving CES1A1 enzyme. [1]

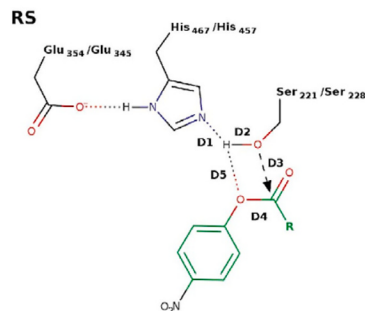
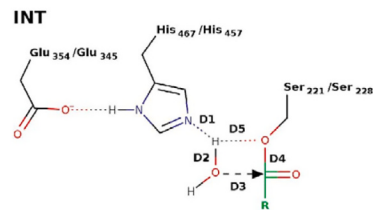
### 2.3.2. Deacylation reaction

The deacylation reaction was studied using the same methodology employed for the acylation reaction where a reaction coordinate involving four distances was employed in an umbrella sampling calculation, with two bonds being formed and two bonds being broken (Fig. 5). The catalytic water hydrogen atom approached the catalytic His nitrogen atom (D1, Fig. 5) and moved away from its oxygen atom bond (D2, Fig. 5). Simultaneously, the water oxygen atom attacks the

carbonyl carbon atom of the acylated Ser until a covalent bond is formed (D3, Fig. 5) and the ester bond between the oxygen atom and the carbonyl carbon atom from the acylated Ser moves away, resulting in breaking this covalent bond (D4, Fig. 5). Again for this reaction, four bond distances were combined linearly, spanning from -4.0 to 4.0 range, to generate the reaction coordinate (RC) analysis according with eq. 1. The four distances were monitored during the course of the deacylation reaction for the whole set of analyzed substrates (D1, D2, D3 and D4, respectively, Figs. S13b, S13d, S14b and 14d).

Only one transition state ( $TS_2$ ) was present in the deacylation reaction, starting from the previous INT state and finishing in the products state (PS) with the release of the corresponding acid and deacylated enzyme (Fig. 5). From the INT state, a water molecule replace the position of the leaving alcohol molecule. Figs. S13b, S13d, S14b and S14d showed that D1 decreases the length until reaching  $TS_2$  (RC ~0.5 to 1.0) with a shortest distance of ~1.1 Å. Meanwhile, the distances between the carbonyl carbon atom and both oxygen atoms (water oxygen and ester oxygen atoms) were ~1.9 Å and ~1.4 Å, D3 and D4, respectively. As was described for the acylation reaction, no covalent bond was formed between the carbonyl carbon and the oxygen atoms, indicating that the deacylation reaction also occurred following a concerted process, where one C—O bond is formed by nucleophilic attack and a second C—O bond was broken simultaneously. [1]

In order to determine the free-energy involved in the hydrolysis reaction of the studied NPE with both CES, the potential of mean force (PMF) was calculated with the combination of the acylation and deacylation processes based on the MD QM/MM(SCC-DFTB3: Amberff14SB) calculations. Before starting with the PMF analysis, the NPE geometries obtained from the docking studies were superimposed

**1) Acylation****2) Deacylation**

**Fig. 5.** Acylation and deacylation reaction pathways for CES1A1 and CES2A1 catalyzed hydrolysis of the ester ligands. NPE derivatives were used as example. Reactant state (RS), first transition state (TS<sub>1</sub>), intermediate (INT), second transition state (TS<sub>2</sub>) and product state (PS).

with the corresponding geometries of the reagent windows of every PMF. Figure S15 shows that for all the NPE substrates their oxygen atom from the carbonyl group is further away from the oxyanion hole in the docking geometries respect to the reagent windows. This result is in line with the fact that the reagent geometries must be closer to the Ser residue in order to start the attack on the substrates carbonyl carbon.

As a result of the PMF calculations, the free-energy profiles are presented in Fig. 6 and the respective energy barriers displayed on Table 2, with their corresponding reported  $k_{\text{cat}}$ . [15] Figs. S16, S17, S18 and S19 show snapshots of the RS, TS, INT and PS geometries belonging to the acylation and deacylation reactions for the NPE substrates with both CES.

These results showed that for the hydrolysis reaction of the two studied NPE performed by both CES, the TS<sub>2</sub> corresponding to the

**Table 2**  
Free-energy of hydrolysis for pNPP and pNPTA on both CES1 and CES2.

Substrate NPE	CES1A1			CES2A1		
	$k_{\text{cat}}$ [15]	TS <sub>1</sub> <sup>a</sup>	TS <sub>2</sub> <sup>a</sup>	$k_{\text{cat}}$ [15]	TS <sub>1</sub> <sup>a</sup>	TS <sub>2</sub> <sup>a</sup>
pNPP	7.9 s <sup>-1</sup>	5.2	10.0	52.5 s <sup>-1</sup>	3.2	6.7
pNPTA	0.4 s <sup>-1</sup>	11.5	12.7	4.4 s <sup>-1</sup>	9.0	10.6

<sup>a</sup> kcal/mol.

deacylation process, is the rate-limiting reaction. The difference on the energetic profile with the TS<sub>1</sub> derived from the presence of the p-nitro group on the structure of the studied NPE, which as an electron-

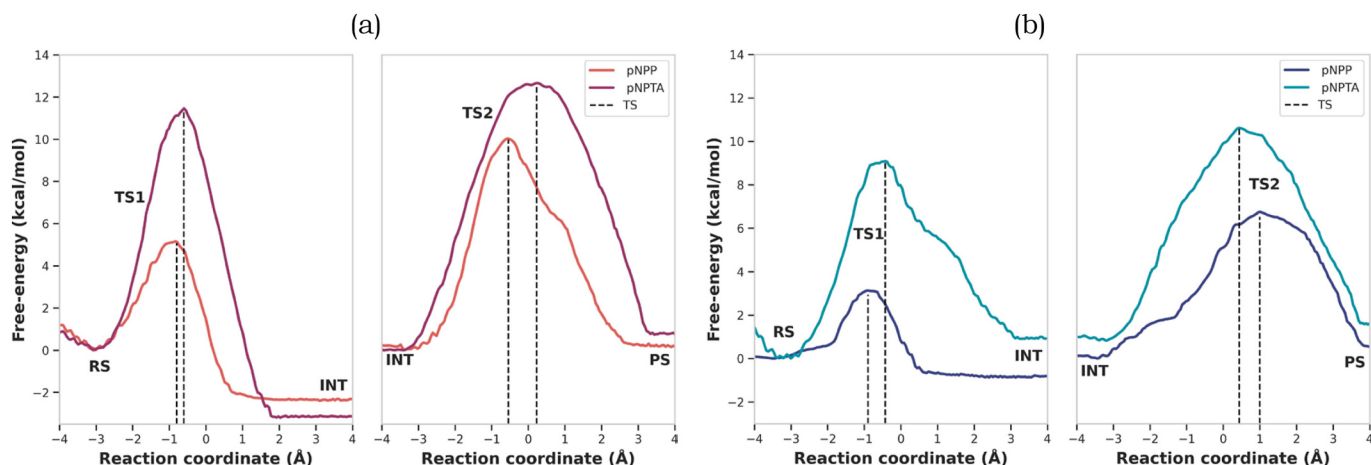


**Fig. 6.** Free-energy profiles for the hydrolysis of pNPP and pNPTA with CES1A1 (a) and CES2A1 (b). The dashed line indicates the corresponding RC for every TS.

withdrawing group, is extracting the electrons from the carbonyl carbon atom, weakening the ester bond present with the oxygen atom of these compounds, resulting in a decrease on the energy of TS<sub>1</sub> respect to TS<sub>2</sub>, during the study of the hydrolysis produced by the CES enzymes. Table 2 shows the information regarding the reported  $k_{\text{cat}}$  [15] and the rate-limiting TS<sub>2</sub> energetic barrier.

Observing the free-energies of activation involved in the hydrolysis of pNPP and pNPTA for both CES, the ester exhibiting the two lowest  $k_{\text{cat}}$  values (i.e. pNPTA,  $k_{\text{cat}} = 0.4\text{s}^{-1}$  and  $4.4\text{s}^{-1}$  for CEA1A1 and CES2A1, respectively) displayed the two highest TS<sub>2</sub> energetic barrier (12.7 kcal/mol and 10.6 kcal/mol, respectively). On the other hand, pNPP exhibits the two highest  $k_{\text{cat}}$  ( $k_{\text{cat}} = 7.9\text{s}^{-1}$  and  $52.5\text{s}^{-1}$  for CEA1A1 and CES2A1, respectively) and was found to exhibit the lowest TS<sub>2</sub> energetic barriers (10.0 kcal/mol and 6.7 kcal/mol, respectively).

In order to unveil the hydrolysis reaction differences between CES1A1 and CES2A1 PMF profiles, the deacylation reaction structures resulting from the QM/MM simulations were further analyzed. In the studied deacylation reactions, the increase in the free-energy of reaction was accompanied by a higher degree of steric hindrance, elicited by the acyl moiety present in the acetylated Ser residue in the respective CES.

Figure S20a and S20b show that the distance between the trimethyl acetate moiety and the attacking water oxygen atom is shorter during the deacylation reaction of pNPTA, than the propyl moiety and the water oxygen atom for the corresponding pNPP, during their deacylation reactions for CES1A1 and CES2A1, respectively. These graphics evidenced that the increase in the energetic barrier of the TS<sub>2</sub> of pNPTA respect to pNPP is probably originated in a higher steric hindrance of the bulky trimethyl acetate moiety present on the pNPTA structure respect to the smaller propyl group present on the pNPP.

After analyzing and successfully approximating the NPE substrate binding affinities and the hydrolytic reaction to their respective CES1A1 and CES2A1 reported kinetic parameters ( $K_M$  and  $k_{\text{cat}}$ , respectively), the applied combination of in silico classical MM strategies and hybrid QM/MM-MD simulations were further extended to the study of substrates exhibiting an isoenzyme stereoselectivity behavior, as is presented in the next sections.

#### 2.4. Modeling of the substrate specificity between CES isoforms and Pyr stereoisomers

##### 2.4.1. Selection of Pyr substrates

In this second stage, the already mentioned in silico protocol was applied to the study of a second set of substrates, formed by two pyrethroid-like fluorescent surrogates stereoisomers (Pyr, Fig. 7) [14]. As can be seen, a strong dependence on the chiral center configuration is observed with respect to the CES mediated hydrolytic efficiency, with Pyr1 exhibiting selectivity towards CES1A1 over CES2A1 in contraposition of Pyr2 that displayed selectivity towards CES2A1 over CES1A1 (Fig. 7). In this way, these two compounds represent excellent molecular probes in which the overall size of the acyl and alkyl moieties are

conserved, anticipating that the three-dimensional positioning within the catalytic site drives the reaction efficiency.

Substrate	$K_M^a$		$k_{\text{cat}}^b$		$k_{\text{cat}}/K_M^c$	
	CES1A1	CES2A1	CES1A1	CES2A1	CES1A1	CES2A1
Pyr1	$0.7 \pm 0.4$	$2.8 \pm 0.1$	$4.4 \pm 0.6$	$0.48 \pm 0.0$	$6.6 \pm 0.03$	$0.17 \pm 0.01$
Pyr2	$2.4 \pm 0.8$	$3.8 \pm 0.4$	$1.7 \pm 0.4$	$4.6 \pm 0.3$	$0.71 \pm 0.03$	$1.2 \pm 0.1$

<sup>a</sup> $\mu\text{M}$ .<sup>b</sup> $\text{m}^{-1}\cdot\text{c m}^{-1}\text{mM}^{-1}$ .

##### 2.4.2. Human CES1 and CES2 substrates binding

In the first stage, the described molecular docking procedure was applied to the Pyr substrates on both CES isoforms, in order to study the binding recognition and the corresponding intermolecular interactions.

First, the results corresponding to the docking of both Pyr derivatives to CES1A1 were analyzed. It was observed that both lowest energy docked poses exhibited homologous spatial disposition within the active site cavity than the previous NPE derivatives, placing the carbonyl oxygen of the hydrolyzable ester moiety in the region corresponding to the oxyanion hole (subpocket 2), thus establishing hydrogen bond interactions with the corresponding residues (Figure S21 and S22). Noteworthy, both the acyl and alkyl moieties were placed within subpocket 1, establishing hydrophobic interactions with the enzyme (Figure S21 and S22). As can be seen the difference in the spatial orientation of the acyl moiety caused by the quiral center is compensated by the relatively high volume of subpocket 1 in CES1A1. When the docking of these two stereoisomers to CES2A1 was analyzed, again both substrates placed their carbonyl oxygen within the oxyanion as was observed for CES1A1, however the two enantiomers exhibited different binding modes. In this case Pyr1 accommodates its alkyl moiety within the subpocket 2 of the active site, while the acyl and nitrile moieties were positioned within subpocket 1 (Figure S23). In counterpart, Pyr2 maintained a similar spatial disposition to that observed for CES1A1, including all its molecular structure within subpocket 1 (Figure S24).

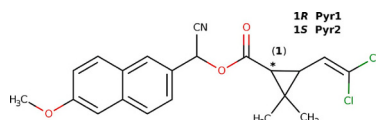
Continuing with the binding analysis protocol, all CES-Pyr complexes were subjected to explicit solvent classic MD simulations, in order to study their intermolecular interaction properties. Figs. S25a and S25b show the distances between the center of mass of the CES1A1 and CES2A1 catalytic binding site residues and the studied substrates, respectively. This analysis displayed that both Pyr substrates maintained their position within both CES catalytic sites during the 100 ns of production stage. Again, as was the case for NPE ligands, the increase in the distances between CES2A1 respect to CES1A1 is because of the larger size of CES2A1 active site. With these CES-Pyr MD simulations, further free-energy of binding interaction (MMGBSA) analyses were applied.

##### 2.4.3. Free-energy interaction analysis

Table 3 shows the free-energy binding interaction analysis on the MD trajectories of Pyr-CES complexes. In the analysis with both CES, Pyr1 displayed slightly higher total free-energy of interaction ( $\Delta G_{\text{Total}}$ ) than Pyr2, which is in agreement with the reported affinity constant ( $K_M$ ) data. [14] The presence of larger hydrophobic moieties on the structure of the Pyr derivatives respect to the NPE increase the VDW interaction, producing the higher affinity properties observed for that family of compounds with both CES isoforms, indicating again the important contribution of the VDW component of interaction in the ligand-CES complex formation.

Continuing with the free-energy interaction analysis, the per-residue decomposition analysis was also performed in the Pyr-CES complexes. Pyr derivatives showed a similar pattern of interaction with residues from CES1A1, displaying the main interactions with the hydrophobic residues Leu304, Leu318, Leu358, Ile359, Leu362, Met363 and Phe425 from subpocket 1 (Figs. 8a, S16 and S17). The per-residue decomposition analysis showed higher free-energy interactions displayed by Pyr compounds with subpocket 1 residues compare to NPE substrates.

The observed interaction pattern changes on the Pyr1-CES2A1 complex because this pyrethroid-like substrate places the acyl moiety on the subpocket 2 section of CES2A1 active site, displaying the main



Substrate	$K_M^a$	$k_{\text{cat}}^b$		$k_{\text{cat}}/K_M^c$	
	CES1A1 CES2A1	CES1A1 CES2A1	CES1A1 CES2A1	CES1A1 CES2A1	CES1A1 CES2A1
Pyr1	$0.7 \pm 0.4$	$2.8 \pm 0.1$	$4.4 \pm 0.6$	$0.48 \pm 0.0$	$6.6 \pm 0.03$
Pyr2	$2.4 \pm 0.8$	$3.8 \pm 0.4$	$1.7 \pm 0.4$	$4.6 \pm 0.3$	$0.71 \pm 0.03$

<sup>a</sup> $\mu\text{M}$ .<sup>b</sup> $\text{m}^{-1}\cdot\text{c m}^{-1}\text{mM}^{-1}$ .

**Fig. 7.** Molecular structure of the pyrethroid-like stereoisomers substrates (Pyr) with their respective CES kinetic parameters. [14].

**Table 3**

Free-energy interaction analysis for Pyr derivatives on both CES1A1 and CES2A1.

Enzyme	Substrate	$K_M^a$	VDW <sup>b</sup>	ELE <sup>c</sup>	$\Delta G_{\text{nonpolar}}^d$	$\Delta G_{\text{polar}}^e$	$\Delta G_{\text{Total}}^f$
CES1A1	Pyr1	0.7	-49.0±2.9	-13.8±4.1	-7.1±0.1	30.5±3.3	-39.5±4.6
	Pyr2	2.4	-50.1±3.2	-7.0±2.8	-7.0±0.1	25.8±2.4	-38.3±3.8
CES2A1	Pyr1	2.8	-55.4±2.6	-23.5±2.2	-7.1±0.1	42.2±2.2	-43.9±3.3
	Pyr2	3.8	-53.7±2.3	-16.2±3.4	-7.1±0.1	35.2±2.9	-41.8±4.0

<sup>a</sup>μM. <sup>b</sup> Van der Waals contribution (kcal/mol). <sup>c</sup>Electrostatic contribution (kcal/mol). <sup>d</sup>Solvation non-polar contribution (kcal/mol). <sup>e</sup>Solvation polar contribution (kcal/mol). <sup>f</sup>Total binding free-energy (kcal/mol).

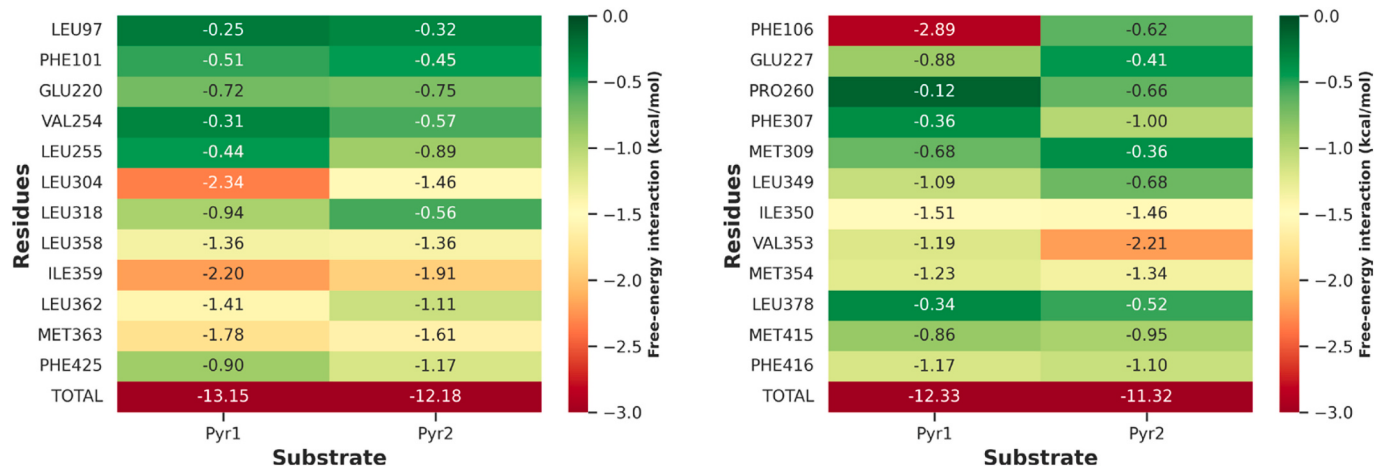


**Fig. 8.** Per-residue free-energy decomposition analysis heatmap from the CES1A1-Pyr (a) and CES2A1-Pyr complexes (b).

interaction with residue Phe106 (Figs. 8b and S18). This interaction pattern is similar to that observed for the NPE-CES2A1 complexes (Fig. 4b), with the exception that Pyr1 displayed stronger interactions with the residues from subpocket 1. Meanwhile, Pyr2 maintained a similar interaction pattern than CES1A1, contacting residues from CES2A1 subpocket 1 (Phe307, Ile350, Val353, Met354, Met415 and Phe416, Figs. 8b and S19).

These results show that Pyr1, in contraposition of Pyr2, was able to change its binding interaction pose, from CES1A1, in order to preserve a high affinity for CES2A1. This variation in the binding conformation impacted positively in the total free-energy of interaction and the reported  $K_M$  for Pyr1-CES2A1 complex.

## 2.5. Hybrid QM/MM simulation of Pyr substrates

In this final section, the study of the potential free-energy involved in the hydrolysis reaction of Pyr derivatives with both CES enzymes was studied. In analogy with the previous study with the NPE ligands, a two steps hydrolysis mechanism was followed: 1) acylation (Figs. S26a, S26c, S27a and S27c) and 2) deacylation (Figs. S26b, S26d, S27b and S27d) reactions (Fig. 5).

Following the same protocol used for the NPE derivatives, the PMF was calculated with the combination of the acylation and deacylation processes, in order to determine the free-energy involved in the hydrolysis reaction of the studied Pyr substrates with both CES. Again in this case, the Pyr geometries obtained from the docking studies were

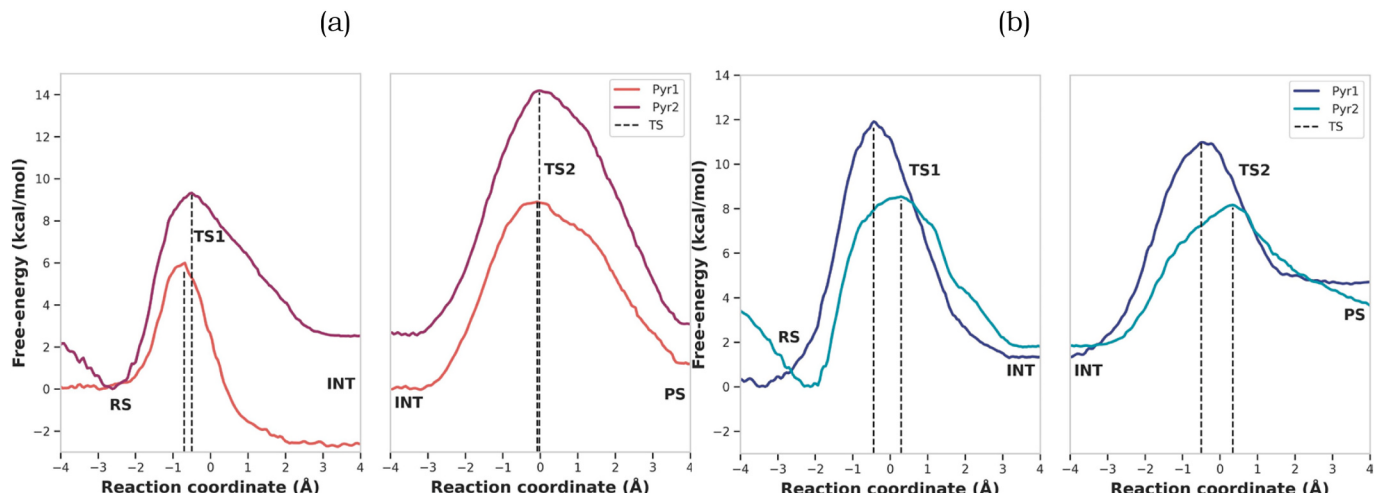


**Fig. 9.** Free-energy profiles for the hydrolysis of Pyr1 and Pyr2 with CES1A1 (a) and CES2A1 (b). The dashed line indicates the corresponding RC for every TS.

superimposed with the corresponding geometries of the reagent state windows of every PMF. Figure S28 shows that in both studied Pyr substrates the docking and reagent state geometries display similar conformation.

As a result of the calculated PMF, the free-energy graphics were plotted in Fig. 9 and the respective energy barriers displayed on Table 4, with their corresponding reported  $k_{cat}$ . [14] Figs. S29, S30, S31 and S32 show snapshots of the RS, TS, INT and PS geometries belonging to the acylation and deacylation reactions for the Pyr substrates with both CES.

These results show a different hydrolysis behavior between the Pyr substrates and both CES isoforms. In the study with CES1A1, the TS<sub>2</sub>, corresponding to the deacylation process is the rate-limiting step of the hydrolysis reaction (Table 4), as was also the case for the studied NPE with both CES. On the other hand, TS<sub>1</sub> showed the highest free-energy values for the CES2A1 hydrolysis reaction, corresponding the acylation process to the rate-limiting transition state of this reaction (Table 4).

Table 4 shows that the experimental differences observed between the stability of the studied Pyr substrates in presence of CES1A1 and CES2A1 was consistent with the calculated rate-limiting free-energy profile of hydrolysis. First, Pyr1 displayed a lower  $k_{cat}$  between CES1A1 and CES2A1 ( $4.4\text{m}^{-1}$  and  $0.48\text{m}^{-1}$ , respectively) corresponding with an increase in the calculated rate-limiting free-energy barriers (8.9 kcal/mol and 12.0 kcal/mol). Pyr2 followed a similar trend, showing higher  $k_{cat}$  values for CES1A1 and CES2A1 ( $1.7\text{m}^{-1}$  and  $4.6\text{m}^{-1}$ , respectively) consistent with the lower rate-limiting free-energy barriers (14.1 kcal/mol and 8.5 kcal/mol).

In order to unveil the hydrolysis reaction differences between CES1A1 and CES2A1 PMF profiles, the structures resulting from the QM/MM simulations for every rate-limiting stage Pyr hydrolysis reaction were further analyzed. As was described in the previous study of the free-energy profiles of NPE, the increase in the free-energy of reaction for the Pyr substrates was accompanied by a higher degree of steric hindrance. In this case, the increase in the steric hindrance was produced by the most bulky moiety in the structure of the Pyr derivatives, the dichloroethylene (DCET).

Starting with the hydrolysis reaction produced by CES1A1, Pyr2 displayed the slower reaction rate with a  $k_{cat}$  of  $1.7\text{m}^{-1}$  (Table 4). Both Pyr2 TS displayed higher energetic barriers than the respective TS from Pyr1 hydrolysis reaction, exhibiting TS<sub>2</sub> as the highest energetic barrier with 11.6 kcal/mol (Table 1). The observed increase in this PMF is originated in the fact that during the deacylation reaction, the oxygen from the water molecule attacks the carbonyl carbon in the same plane where the DCET moiety is present, resulting in a TS<sub>2</sub> structure with a high steric hindrance (Video1, Supporting material). On the other hand, the TS<sub>2</sub> structure of Pyr1 was subjected to the attack of the water molecule oxygen on the carbonyl carbon in a different plane than the DCET moiety (Video2, Supporting material), producing a lower energetic barrier (8.9 kcal/mol, Table 4). Figure S33a shows that the distance between the DCET chlorine atom and the attacking water oxygen atom is around 3 Å for the deacylation reaction of Pyr2, while it is larger (5 Å) for the same reaction stage of Pyr1.

Regarding the hydrolysis reaction mediated by CES2A1, Pyr1 derivative showed the slower reaction rate ( $k_{cat}$  of  $0.48\text{m}^{-1}$ , Table 4) during the acylation reaction stage. As was mentioned in a previous

section, Pyr1 changes the binding pose for the interaction with the active site of CES2A1 respect to the binding pose on CES1A1, placing the acyl and nitrile moieties within subpocket 1 (Figure S23). Considering that the DCET group is part of the acyl moiety of the Pyr molecule, both DCET and nitrile moieties were inside subpocket 1. The simulation during the acylation reaction showed that the mentioned moieties were in a very close distance (Video3, Supporting material), approximately 3 Å (Figure S33b), producing a high steric hindrance with the corresponding increase in the energetic barrier (12.0 kcal/mol, Table 4). Pyr2 displayed an acylation reaction simulation with a longer distance between the DCET and nitrile moieties (Video4, Supporting material), around 6 Å (Figure S33b), generating lower steric hindrance with the corresponding lower energetic barrier (8.5 kcal/mol, Table 4).

### 3. Conclusion

The objective of this work was to explore the selectivity observed for the main CES isoforms, CES1A1 and CES2A1, over two family of substrates. In order to accomplish this objective, a molecular modeling protocol was developed, combining classical modeling simulation strategies with hybrid QM/MM MD simulations, for approximating the reported affinity constant ( $K_M$ ) and enzymatic turn-over ( $k_{cat}$ ) of a group of two different sets of substrates.

In a first stage, the molecular modeling protocol was used to study a set of 5 NPE derivatives with well known reported enzymatic parameters ( $K_M$  and  $k_{cat}$ ). The classical molecular modeling studies showed a trend between the reported affinity properties and the total free-energy of interaction of these substrates. In addition, the van der Waals (VDW) component of interaction, with the hydrophobic residues present on CES1A1 and CES2A1 subpocket 2 and subpocket 1, showed a significant contribution to the NPE-CES interaction. Moreover, the hybrid QM/MM MD simulations exhibited that the rate-limiting step for the studied NPE reactions were related to the TS with the higher steric hindrance molecular structure produced during the course of the deacylation reactions. Overall, the developed molecular modeling protocol displayed good approximations to describe both enzymatic parameters of the NPE family set with CES1A1 and CES2A1.

With the previously mentioned molecular modeling protocol, in a second stage, a set of two pyretroid-like stereoisomers were used. The classical molecular modeling studies showed again a trend between the total free-energy of interaction and the reported  $K_M$ . This study also exhibited that the increase in the cavity volume of CES2A1 respect to CES1A1 allowed Pyr1 to display a differential interaction pattern, interacting with residues from subpocket 2 and subpocket 1, and maintaining a higher affinity for CES2A1 than Pyr2.

Meanwhile, the hybrid QM/MM MD simulations also showed that the rate-limiting step for the studied Pyr reactions were related to the TS with the higher steric hindrance molecular structure, which for the Pyr derivatives is the DCET moiety. In addition, the previously mentioned change in the interaction pattern for Pyr1 in complex with CES2A1 produced an increase in the energetic barrier in the rate-limiting TS for this reaction, translating in the slower catalytic turn-over of all the studied reactions.

Overall, it was possible to observe that the studied substrates initially generate the best possible interaction pattern, with the residues of the respective CES catalytic cavity, in order to produce the highest possible affinity constant with the enzyme. Then, this interaction pattern drives the catalytic turn-over reaction through the presence or absence of a high steric hindrance center in the molecular structure of the rate-limiting reaction.

In conclusion, the selectivity of the CES isoforms is not only related to the molecular size of the alkyl or acyl groups of the substrates, but a more complex scenario driven by the initial conformation of the substrate in the interaction with the CES active site.

**Table 4**  
Free-energy of hydrolysis for Pyr1 and Pyr2 on both CES1A1 and CES2A1.

Substrate	CES1A1			CES2A1		
	$k_{cat}$	TS <sub>1</sub> <sup>a</sup>	TS <sub>2</sub> <sup>a</sup>	$k_{cat}$	TS <sub>1</sub> <sup>a</sup>	TS <sub>2</sub> <sup>a</sup>
Pyr1	$4.4\text{ m}^{-1}$	6.0	8.9	$0.48\text{ m}^{-1}$	12.0	10.9
Pyr2	$1.7\text{ m}^{-1}$	9.3	14.1	$4.6\text{ m}^{-1}$	8.5	8.0

<sup>a</sup> kcal/mol.

## 4. Methods

### 4.1. Structures preparation and pocket analysis

The crystallographic structure PDB code 5A7F (1.86 Å resolution) [30] was used as starting point for the preparation of CES1A1 structure. Considering that CES1A1 can exist as a multimeric specie, in this work only the A-chain was selected since the objective of the work was focused on modeling substrate binding and hydrolysis, event that depends on the pharmacodynamic events taking place within the corresponding catalytic site. It should be mentioned that no structural interaction between the mentioned catalytic sites of different chains in the multimeric specie is expected, since upon superimposition of the monomeric structure of CES1A1 onto the corresponding trimeric crystallographic structure no evident interaction was observed (Figure S34). Finally, the water molecules and non-peptidic residues were deleted prior to receptor preparation.

Since the crystal structure of CES2A1 has not been resolved, the best homology model structure was retrieve from a list of models already available in the server (<https://swissmodel.expasy.org/>) based on the template structure of CES1A1 (PDB code 5A7G, 1.48 Å resolution). [30] The QMEAN scoring function was used to validate the structure model showing a value of -2.30. Both enzymes were processed previous to the docking study with the *pd4amber* tool from Amber20 package. [31]

Upon structural inspection of the catalytic triad conformation in both receptor models, it was observed that they corresponded to an activated conformation, which was considered as adequate for the sake of the studies performed, and thus was used without further structural refinement during molecular docking studies.

Pocket volume was calculated with *POVME2* software [29] with 1 Å grip spacing and 0.9 Å of distance cutoff. The center of the inclusion sphere were determine based on the catalytic Serine oxygen atom coordinate with a 12 Å radius.

### 4.2. Molecular docking procedures

The molecular structure of the substrates started as a list SMILES that were converted to three-dimensional structure with Obabel software. [32] For every compound 100 different conformation were generated applying a minimization protocol by considering the Merck Molecular Force Field (MMFF94) [33] implemented in RDKit. [34] From this analysis, the lowest energy conformation was selected to calculate the restrained electrostatic potential (RESP) charges using HF method and 6-31G\* basis set executed in Gaussian09. [35]

Molecular docking studies were performed using *DOCK6* software. [36] Spheres defining the active binding site were generated using the *SPHGEN* utility, considering a box that includes all the residues that have been reported as part of the binding site and allowing a 5.0 Å extra margin in all directions. The receptor binding site surface was calculated using the *DMS* open source tool, and the corresponding docking grid was generated using the *grid* module contained in *DOCK6* applying default parameter values. For the docking procedure, a minimum anchor size of 5 atoms was selected, with a maximum of 1000 anchor orientations being generated. Ligand positions were minimized during growth with a simplex minimizer (500 iterations, 1.0 kcal mol<sup>-1</sup>). A maximum of 500 conformers were kept for each ligand and afterwards clustered (2.0 Å RMSD) and docked within the corresponding box. The primary docking score was based on the standard grid-based energy scoring, while the secondary score was a descriptor-based scoring function using pharmacophore matching descriptors. The best score resulting from both descriptor functions was selected for further analysis, with visual inspection being performed using the *LigPlot+* software. [37]

### 4.3. Molecular dynamics (MD) simulations

The MD simulations were performed with *pmemd.cuda* tool from Amber20 software package. [31] The protein was parameterized using the ff14SB force field [38]. The identified ionizable residues within the catalytic region are His467/457 and Glu354/345 (catalytic triad) and Glu220/227, which is located between subpockets 2 and 3. The ionization states of the former ones were assumed as previously reported for the *charge relay system* associated to the general catalytic mechanism of serine protease enzymes. [39,40] Consequently, the Glu residue was considered to exist in its ionized state (pH 7.4), while the His residue was modeled with the corresponding proton positioned in the delta nitrogen (HID), and interacting with the carboxylate group of the nearby Glu residue. Respect to Glu220/227, it was also modeled in its ionized state after considering its sidechain pKa value (4.25) and the modeled physiological conditions (pH 7.4). The ligands were parameterized with the GAFF force field. [41] Complexes were solvated using a pre-equilibrated TIP3PBOX solvent box, with boundaries constructed at a minimum distance of 10 Å. Standard minimization procedures were applied: first stage of 5000 steps maintaining the solute restrained and a second stage of 5000 steps with restraints on the backbone of the protein. After minimization, a heating stage of the solvent (0.5 ns, 298° K) was performed under constant volume conditions and applying restraint on the solute. Equilibration runs (1 ns) were performed with restraints on the protein backbone and production phases (100 ns) were performed under constant pressure (1 atm) and temperature conditions (298° K) matching the one used in the experimental determinations of the kinetic parameters used as reference. Since the C-terminal section in both the crystallographic CES1A1 and the model CES2A1 structures was missing, MD simulation were performed applying restraints in the enzyme backbone (5 kcal mol<sup>-1</sup> Å<sup>2</sup>) in order to avoid the disruption of the tertiary structure during the simulations. All MD simulations, were performed under periodic boundary conditions, the time step was 2 fs, with the SHAKE algorithm [42] being used for the hydrogen atoms and a 8 Å cutoff value applied to compute the non-bounded interactions. From the mentioned equilibration stage, two independent 100 ns production runs were performed: 1) the first one with a distance constraints (400 kcal mol<sup>-1</sup> Å<sup>2</sup>) apply on several hydrogen bond interactions in order to maintain the substrate-CES complexes in a reactive position for the next step of QM/MM simulation. The constrained hydrogen bonds were: a) between the residues of the catalytic triad Glu354/Glu345 and His465/His457, for CES1A1 and CES2A1, respectively; and b) between the residues of the oxianion hole (Gly142, Gly143 and Ala222 on CES1A1 and Gly149, Ala150 and Ala229 on CES2A1) and the carbonyl oxygen of the studied substrates. 2) The second 100 ns production phase was performed without hydrogen bond distance restraints between the oxianion hole residues and the substrates, and the generated trajectory was used to perform the corresponding binding free energy decomposition analysis displayed in the next section. Figure S35 show the computed RMSD of the complete CES1A1 and CES2A1 enzymes for both production runs. Visual inspection of the MD trajectories was performed using the VMD v.1.9.3 software. [43]

### 4.4. Binding free energy decomposition analysis

The Molecular Mechanics generalized Born surface area (MMGBSA) method implemented in the MMPBSA.py script, [44] included in Amber20 package, [31] was used to calculate the free-energy of interaction between the studied esters and the catalytic site residues of both CES. The whole production trajectory without the hydrogen bond constraints (production phase 2 from section 4.3), was included in this analysis, with the electrostatic (ELE), van der Waals (vdW) and total interaction energies being computed. In addition, per-residue interaction decomposition was performed to quantitatively identify the more relevant residues contacts. The binding energy was estimated by taking

into account the solvation energies of the interacting molecules and the molecular mechanics (MM) energies. The contribution of polar solvation energies was computed applying the generalized Born (MMGBSA) implicit solvent model, while the non-polar contribution of the solvation energy was dependent on the solvent accessible surface area.

#### 4.5. Hybrid QM/MM simulations

The ligand-enzyme system was divided into quantum and classical regions for the QM/MM simulation. The QM region comprised for the acylation reaction: the catalytic triad (side chains of residues Ser221/Ser228, His465/His457 and Glu354/Glu345) and the structure of the ligand (Pyr and NPE derivative); and for the deacylation reaction: the catalytic triad (with the acylated serine residue) and the water molecule (Figure S36). The water molecule in the deacylation reaction was added using the oxygen atom from the leaving alcohol originated in the previous acylation reaction as reference. This region was parameterized with the self-consistent-charge density-functional tight-binding method (SCC-DFTB3). [45–47] This method was selected based on previous reports in which QM/MM studies were performed for these enzymes. [1] The classical region was treated with Amber ff14SB force field, along with the TIP3P water model. The QM/MM simulation were conducted with the module *sander* from Amber20 package. [31]

First, a QM/MM simulation of 100 ps was performed, with the previous mentioned constraint distance on the hydrogen bond interaction, starting from the classical MD constraint production coordinates (production phase 1 from section 4.3). From the last step of this simulation, the reaction coordinate calculation was started. Umbrella sampling (US) simulations were applied to generate the reaction free energy profile (for both acylation and deacylation reactions) following a linear combination of distances (LCOD) with values from  $-4.0 \text{ \AA}$  to  $4.0 \text{ \AA}$ , to generate the reaction coordinate (RC) analysis according with eq. 1. The harmonic potential used for the LCOD was  $200 \text{ kcal mol}^{-1} \text{ \AA}^2$ . The US simulations were divided in 80 windows with interval of  $0.1 \text{ \AA}$ . For each window, 5 ps of equilibration followed by 30 ps of production were performed, with a time step of 1 fs at  $298 \text{ K}$ . The free-energy profiles were obtained from all the adjacent overlapping windows belong to every production QM/MM simulation stage (Figs. S37 and S38), using the vFEP software. [48]

Supplementary data to this article can be found online at <https://doi.org/10.1016/j.bbapap.2025.141069>.

#### Funding

This research was supported by grants from the Agencia Nacional de Promoción Científica y Tecnológica FONCYT PICT-2019-03461 and the Consejo Nacional de Investigaciones Científicas y Técnicas (CONICET).

#### CRediT authorship contribution statement

**Sergio R. Ribone:** Writing – review & editing, Writing – original draft, Visualization, Validation, Methodology, Investigation, Formal analysis, Conceptualization. **Dario A. Estrin:** Writing – review & editing, Writing – original draft, Supervision, Methodology, Formal analysis, Conceptualization. **Mario A. Quevedo:** Writing – review & editing, Writing – original draft, Supervision, Resources, Project administration, Methodology, Investigation, Funding acquisition, Formal analysis, Conceptualization.

#### Declaration of competing interest

The authors declare that they have no known competing financial interests or personal relationships that could have appeared to influence the work reported in this paper.

#### Acknowledgements

Authors acknowledge the Centro de Computación de Alto Desempeño (CCAD, <https://supercomputo.unc.edu.ar/>) , Universidad Nacional de Córdoba, Córdoba, Argentina, for providing computing resources for this work.

#### Data availability

Data will be made available on request.

#### References

- [1] J. Yao, X. Chen, F. Zheng, C.-G. Zhan, Catalytic reaction mechanism for drug metabolism in human carboxylesterase-1: cocaine hydrolysis pathway, *Mol. Pharm.* 15 (9) (2018) 3871–3880.
- [2] P.R. Figueiredo, R.D. González, A.T. Carvalho, Human carboxylesterase 2 in cocaine metabolism, *Mol. Catal.* 515 (2021) 111938.
- [3] T. Fukami, T. Yokoi, The emerging role of human esterases, Drug metabolism and pharmacokinetics (2012) DMPK-12.
- [4] D. Wang, L. Zou, Q. Jin, J. Hou, G. Ge, L. Yang, Human carboxylesterases: a comprehensive review, *Acta Pharm. Sin. B* 8 (5) (2018) 699–712.
- [5] Y.-Q. Song, Q. Jin, D.-D. Wang, J. Hou, L.-W. Zou, G.-B. Ge, Carboxylesterase inhibitors from clinically available medicines and their impact on drug metabolism, *Chem. Biol. Interact.* 345 (2021) 109566.
- [6] M. Takahashi, I. Hirota, T. Nakano, T. Kotani, D. Takami, K. Shiratori, Y. Choi, M. Haba, M. Hosokawa, Effects of steric hindrance and electron density of ester prodrugs on controlling the metabolic activation by human carboxylesterase, *Drug Metab. Pharmacokinet.* 38 (2021) 100391.
- [7] J. Lian, R. Nelson, R. Lehner, Carboxylesterases in lipid metabolism: from mouse to human, *Protein Cell* 9 (2) (2018) 178–195.
- [8] M.K. Ross, T.M. Streit, K.L. Herring, S. Xie, Carboxylesterases: dual roles in lipid and pesticide metabolism, *J. Pestic. Sci.* (2010) 1006090136.
- [9] S. Bencharit, C.C. Edwards, C.L. Morton, E.L. Howard-Williams, P. Kuhn, P. M. Potter, M.R. Redinbo, Multisite promiscuity in the processing of endogenous substrates by human carboxylesterase 1, *J. Mol. Biol.* 363 (1) (2006) 201–214.
- [10] T. Imai, Human carboxylesterase isozymes: catalytic properties and rational drug design, *Drug Metab. Pharmacokinet.* 21 (3) (2006) 173–185.
- [11] M. Hosokawa, Structure and catalytic properties of carboxylesterase isozymes involved in metabolic activation of prodrugs, *Molecules* 13 (2) (2008) 412–431.
- [12] G.F. Makhaeva, S.V. Lushchekina, N.P. Boltneva, O.G. Serebryakova, N. V. Kovaleva, E.V. Rudakova, N.A. Elkina, E.V. Shchegolkov, Y.V. Burgart, T. S. Stupina, et al., Novel potent bifunctional carboxylesterase inhibitors based on a polyfluoroalkyl-2-imino-1, 3-dione scaffold, *Eur. J. Med. Chem.* 218 (2021) 113385.
- [13] G. Vistoli, A. Pedretti, A. Mazzolini, B. Testa, Homology modeling and metabolism prediction of human carboxylesterase-2 using docking analyses by gridock: a parallelized tool based on autodock 4.0, *J. Comput. Aided Mol. Des.* 24 (9) (2010) 771–787.
- [14] K. Nishi, H. Huang, S.G. Kamita, I.-H. Kim, C. Morisseau, B.D. Hammock, Characterization of pyrethroid hydrolysis by the human liver carboxylesterases hce-1 and hce-2, *Arch. Biochem. Biophys.* 445 (1) (2006) 115–123.
- [15] M. Hatfield, L. Tsurkan, J. Hyatt, X. Yu, C. Edwards, L. Hicks, R. Wadkins, P. Potter, Biochemical and molecular analysis of carboxylesterase-mediated hydrolysis of cocaine and heroin, *Br. J. Pharmacol.* 160 (8) (2010) 1916–1928.
- [16] T. Fukami, M. Kariya, T. Kurokawa, A. Iida, M. Nakajima, Comparison of substrate specificity among human arylacetamide deacetylase and carboxylesterases, *Eur. J. Pharm. Sci.* 78 (2015) 47–53.
- [17] M. Takahashi, T. Uehara, M. Nonaka, Y. Minagawa, R. Yamazaki, M. Haba, M. Hosokawa, Synthesis and evaluation of haloperidol ester prodrugs metabolically activated by human carboxylesterase, *Eur. J. Pharm. Sci.* 132 (2019) 125–131.
- [18] S. Bencharit, C.L. Morton, Y. Xue, P.M. Potter, M.R. Redinbo, Structural basis of heroin and cocaine metabolism by a promiscuous human drug-processing enzyme, *Nat. Struct. Mol. Biol.* 10 (5) (2003) 349–356.
- [19] D. Yang, X. Wang, Y.-t. Chen, R. Deng, B. Yan, Pyrethroid insecticides: isoform-dependent hydrolysis, induction of cytochrome p450 3a4 and evidence on the involvement of the pregnane x receptor, *Toxicol. Appl. Pharmacol.* 237 (1) (2009) 49–58.
- [20] K.F. McClure, D.W. Piotrowski, D. Petersen, L. Wei, J. Xiao, A.T. Londregan, A. S. Kamlet, A.-M. Dechert-Schmitt, B. Raymer, R.B. Ruggeri, et al., Liver-targeted small-molecule inhibitors of proprotein convertase subtilisin/kexin type 9 synthesis, *Angew. Chem.* 129 (51) (2017) 16436–16440.
- [21] T. Yoshida, T. Fukami, T. Kurokawa, S. Gotoh, A. Oda, M. Nakajima, Difference in substrate specificity of carboxylesterase and arylacetamide deacetylase between dogs and humans, *Eur. J. Pharm. Sci.* 111 (2018) 167–176.
- [22] S. Honda, T. Fukami, T. Tsujiguchi, Y. Zhang, M. Nakano, M. Nakajima, Hydrolase activities of cynomolgus monkey liver microsomes and recombinant ces1, ces2, and aadac, *Eur. J. Pharm. Sci.* 161 (2021) 105807.
- [23] S.E. Pratt, S. Durland-Busbice, R.L. Shepard, K. Heinz-Taheny, P.W. Iversen, A. H. Dantzig, Human carboxylesterase-2 hydrolyzes the prodrug of gemcitabine

- (ly2334737) and confers prodrug sensitivity to cancer cells, *Clin. Cancer Res.* 19 (5) (2013) 1159–1168.
- [24] Y. Li, Y. Liu, Y. Chen, K. Wang, Y. Luan, Design, synthesis and antitumor activity study of a gemcitabine prodrug conjugated with a hdac6 inhibitor, *Bioorg. Med. Chem. Lett.* 72 (2022) 128881.
- [25] J. Pulido, A.J. Sobczak, J. Balzarini, S.F. Wnuk, Synthesis and cytostatic evaluation of 4-n-alkanoyl and 4-n-alkyl gemcitabine analogues, *J. Med. Chem.* 57 (1) (2014) 191–203.
- [26] D. Gilham, S. Ho, M. Rasouli, P. Martres, D.E. Vance, R. Lehner, Inhibitors of hepatic microsomal triacylglycerol hydrolase decrease very low density lipoprotein secretion, *FASEB J.* 17 (12) (2003) 1685–1687.
- [27] D.A. Bachovchin, B.F. Cravatt, The pharmacological landscape and therapeutic potential of serine hydrolases, *Nat. Rev. Drug Discov.* 11 (1) (2012) 52–68.
- [28] J. Zhang, Q.-S. Pan, X.-K. Qian, X.-L. Zhou, Y.-J. Wang, R.-J. He, L.-T. Wang, Y.-R. Li, H. Huo, C.-G. Sun, et al., Discovery of triterpenoids as potent dual inhibitors of pancreatic lipase and human carboxylesterase 1, *J. Enzyme Inhib. Med. Chem.* 37 (1) (2022) 629–640.
- [29] J.D. Durrant, L. Votapka, J. Sørensen, R.E. Amaro, Povme 2.0: an enhanced tool for determining pocket shape and volume characteristics, *J. Chem. Theory Comput.* 10 (11) (2014) 5047–5056.
- [30] V. Arena de Souza, D.J. Scott, J.E. Nettleship, N. Rahman, M.H. Charlton, M. A. Walsh, R.J. Owens, Comparison of the structure and activity of glycosylated and aglycosylated human carboxylesterase 1, *PLoS One* 10 (12) (2015) e0143919.
- [31] D.A. Case, K. Belfon, I.Y. Ben-Shalom, S.R. Brozell, D.S. Cerutti, T.E. Cheatham III, V.W.D. Cruzeiro, T.A. Darden, R.E. Duke, G. Giambasu, M.K. Gilson, H. Gohlke, A. W. Goetz, R. Harris, S. Izadi, S.A. Izmailov, K. Kasavajhala, A. Kovalenko, R. Krasny, T. Kurtzman, T.S. Lee, S. LeGrand, P. Li, C. Lin, J. Liu, T. Luchko, R. Luo, V. Man, K.M. Merz, Y. Miao, O. Mikhailovskii, G. Monard, H. Nguyen, A. Onufriev, F. Pan, S. Pantano, R. Qi, D.R. Roe, A. Roitberg, C. Sagui, S. Schott-Verdugo, J. Shen, C.L. Simmerling, N.R. Skrynnikov, J. Smith, J. Swails, R.C. Walker, J. Wang, L. Wilson, R.M. Wolf, X. Wu, Y. Xiong, Y. Xue, D.M. York, P.A. Kollman, Amber 2020, University of California, San Francisco, 2020.
- [32] N.M. O'Boyle, M. Banck, C.A. James, C. Morley, T. Vandermeersch, G. R. Hutchison, Open babel: an open chemical toolbox, *J. Chemother.* 3 (2011) 1–14.
- [33] T.A. Halgren, Merck molecular force field. i. Basis, form, scope, parameterization, and performance of mmff94, *J. Comput. Chem.* 17 (5–6) (1996) 490–519.
- [34] G. Landrum, et al., Rdkit: a software suite for cheminformatics, computational chemistry, and predictive modeling, *Greg Landrum* 8 (31.10) (2013) 5281.
- [35] M.J. Frisch, G.W. Trucks, H.B. Schlegel, G.E. Scuseria, M.A. Robb, J.R. Cheeseman, G. Scalmani, V. Barone, B. Mennucci, G.A. Petersson, H. Nakatsuji, M. Caricato, X. Li, H.P. Hratchian, A.F. Izmaylov, J. Bloino, G. Zheng, J.L. Sonnenberg, M. Hada, M. Ehara, K. Toyota, R. Fukuda, J. Hasegawa, M. Ishida, T. Nakajima, Y. Honda, O. Kitao, H. Nakai, T. Vreven, J.A. Montgomery, J.E. Peralta, F. Ogliaro, M. Bearpark, J.J. Heyd, E. Brothers, K.N. Kudin, V.N. Staroverov, R. Kobayashi, J. Normand, K. Ragahavachari, A. Rendell, J.C. Burant, S.S. Iyengar, J. Tomasi, M. Cossi, N. Rega, J.M. Millam, M. Klene, J.E. Knox, J.B. Cross, V. Bakken, C. Adamo, J. Jaramillo, R. Gomperts, R.E. Stratmann, O. Yazyev, A.J. Austin, R. Cammi, C. Pomelli, J.W. Ochterski, R.L. Martin, K. Morokuma, V.G. Zakrzewski, G.A. Voth, P. Salvador, J.J. Dannenberg, S. Dapprich, A.D. Daniels, O. Farkas, J. B. Foresman, J.V. Ortiz, J. Cioslowski, D.J. Fox, Gaussian 09 Revision E.01, gaussian Inc., Wallingford CT, 2009.
- [36] W.J. Allen, T.E. Balius, S. Mukherjee, S.R. Brozell, D.T. Moustakas, P.T. Lang, D. A. Case, I.D. Kuntz, R.C. Rizzo, Dock 6: impact of new features and current docking performance, *J. Comput. Chem.* 36 (15) (2015) 1132–1156.
- [37] R.A. Laskowski, M.B. Swindells, Ligplot+: Multiple Ligand-Protein Interaction Diagrams for Drug Discovery, 2011.
- [38] J.A. Maier, C. Martinez, K. Kasavajhala, L. Wickstrom, K.E. Hauser, C. Simmerling, ff14sb: improving the accuracy of protein side chain and backbone parameters from ff99sb, *J. Chem. Theory Comput.* 11 (8) (2015) 3696–3713.
- [39] A. Warshel, G. Naray-Szabo, F. Sussman, J. Hwang, How do serine proteases really work? *Biochemistry* 28 (9) (1989) 3629–3637.
- [40] L. Hedstrom, Serine protease mechanism and specificity, *Chem. Rev.* 102 (12) (2002) 4501–4524.
- [41] J. Wang, R.M. Wolf, J.W. Caldwell, P.A. Kollman, D.A. Case, Development and testing of a general amber force field, *J. Comput. Chem.* 25 (9) (2004) 1157–1174.
- [42] J.-P. Ryckaert, G. Ciccotti, H.J. Berendsen, Numerical integration of the cartesian equations of motion of a system with constraints: molecular dynamics of n-alkanes, *J. Comput. Phys.* 23 (3) (1977) 327–341.
- [43] W. Humphrey, A. Dalke, K. Schulten, Vmd: visual molecular dynamics, *J. Mol. Graph.* 14 (1) (1996) 33–38.
- [44] B.R. Miller III, T.D. McGee Jr., J.M. Swails, N. Homeyer, H. Gohlke, A.E. Roitberg, Mmpbsa.Py: an efficient program for end-state free energy calculations, *J. Chem. Theory Comput.* 8 (9) (2012) 3314–3321.
- [45] M. Gaus, Q. Cui, M. Elstner, Dftb3: extension of the self-consistent-charge density-functional tight-binding method (scf-dftb), *J. Chem. Theory Comput.* 7 (4) (2011) 931–948.
- [46] M. Elstner, D. Porezag, G. Jungnickel, J. Elsner, M. Haugk, T. Frauenheim, S. Suhai, G. Seifert, Self-consistent-charge density-functional tight-binding method for simulations of complex materials properties, *Phys. Rev. B* 58 (11) (1998) 7260.
- [47] G.M. Seabra, R.C. Walker, M. Elstner, D.A. Case, A.E. Roitberg, Implementation of the scf-dftb method for hybrid qm/mm simulations within the amber molecular dynamics package, *Chem. Eur. J.* 111 (26) (2007) 5655–5664.
- [48] T.-S. Lee, B.K. Radak, A. Pabis, D.M. York, A new maximum likelihood approach for free energy profile construction from molecular simulations, *J. Chem. Theory Comput.* 9 (1) (2013) 153–164.